Electronic Supplementary Material (ESI) for Chemical Science.

Supporting Information: Towards Multistate Multimode Landscapes in Singlet Fission of Pentacene: The Dual Role of Charge-Transfer States

Rajat Walia[a], Zexiang Deng[a], and Jun Yang*[a]

[a]Department of Chemistry, The University of Hong Kong, Pokfulam Road, Hong Kong, P.R. China
*juny@hku.hk

S1 Correlating a large active space for DMRG calculation in pentacene dimer

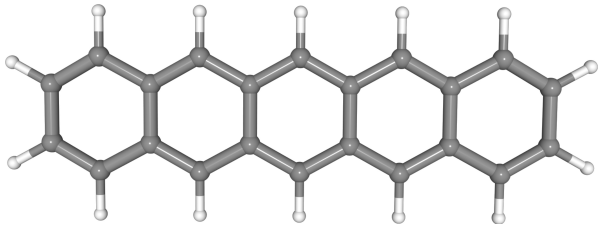

Fig. S1: The pentacene molecule

We calculate the energy ordering for pentacene monomer (Fig. S1) using state-averaged DMRGSCF/NEVPT2 calculations for various active spaces by giving equal weights to the states included in the calculations. Fig. S2 shows that the smaller active spaces such as - 4π4e and 8π8e underestimate the energies of singlet states. However, using the larger active spaces such as: 10-14 π orbitals/electrons provide good agreement with the experimental values.[1] Our calculations indicate that the 'dark state' is not an underlying state as suggested by Zimmerman et al.[2] However, our results are in a good agreement with other theoretical results implying that the S_1 state lies below the S_2 [dark state(D)] state in pentacene monomer.[3,4] A 16π16e active space accurately predicts the singlet state energies but overestimates the S-T gaps in the monomer.

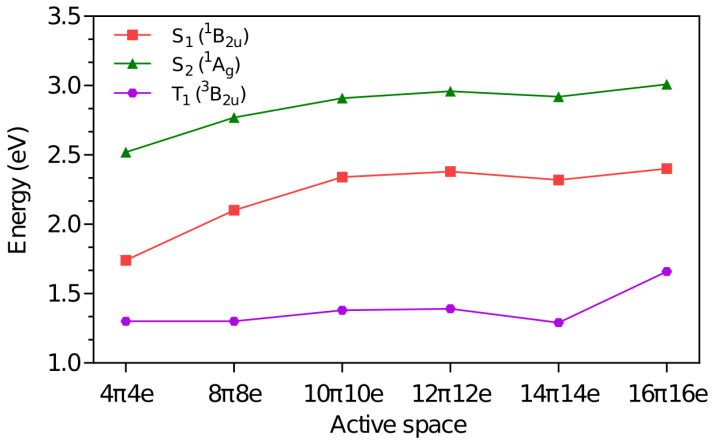

Fig. S2: DMRGSCF/NEVPT2 excited state energies (eV) of the two low-lying excited singlet states and one triplet state of pentacene monomer for a range of active spaces.

We establish that the active spaces of 10-14 π-orbitals/electrons are sufficient for pentacene monomer, accordingly a correlated space of >20 π- orbitals/electrons should be built for the dimer. We benchmark the excited state energies of the dimer for a range of active orbitals/electrons and find the need to correlate at least 22π22e active space to accurately predict the excited states energies of adiabatic states[5] for pentacene dimer (Fig. S2). However, the NEVPT2 correction for bipentacene is computationally demanding for a DMRGSCF(22π22e)/cc-pVTZ calculation and a NEVPT2 correction at DMRGSCF(12π12e)/cc-pVTZ relates to these energies. The wavefunction analysis implemented in this study is based on DMRG state and transition density matrices and only considers the static part of the electronic correlation. It is clear from the Fig. S2 that a

large part of static correlation can be significantly treated by correlating at least 22 electrons, for a given perturbation in the wavefunction. On correlating a larger virtual orbitals space (44π22e), the energies for S_1 and S_2 remain similar to that of a 22π22e active space. So, we use a 22π22e active space in our DMRG calculations.

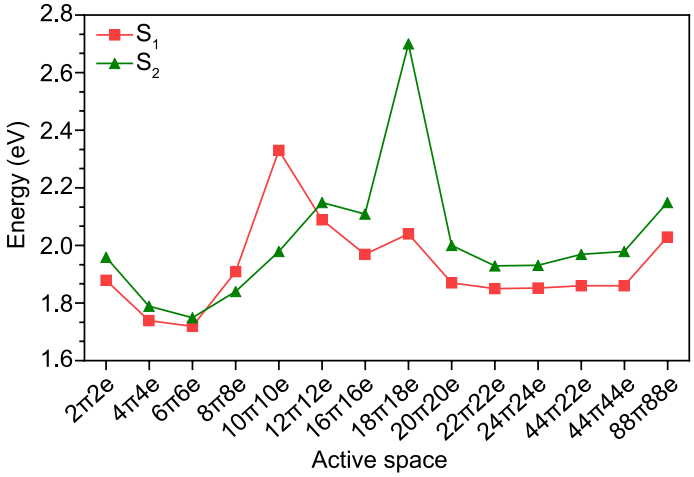

Fig. S3: The DMRGSCF/NEVPT2 excited state energies (eV) of the two low-lying excited singlet states in pentacene dimer for a range of active spaces. A 22π22e active space significantly treats the static correlation in the molecule and yields accurate excited state energies.

The accuracy of DMRG calculation depends on the number of renormalized states (M). Table S1 comprises the energies of three lowest singlet states of pentacene dimer at different M values. M=1000 seems to accurate enough for our system. So, we use M=1000 in our DMRG calculations.

Table S1: DMRGSCF/NEVPT2 energies (E_h) of S_0, S_1, S_2 at different M values for pentacene dimer

M	S_0	S_1	S_2
250	-1688.9115	-1688.8432	-1688.8405
500	-1688.9120	-1688.8441	-1688.8410
800	-1688.9121	-1688.8443	-1688.8414
1000	-1688.9123	-1688.8445	-1688.8414
1500	-1688.9123	-1688.8445	-1688.8414
2000	-1688.9123	-1688.8445	-1688.8414
2500	-1688.9123	-1688.8445	-1688.8414
3000	-1688.9123	-1688.8446	-1688.8415
4000	-1688.9123	-1688.8446	-1688.8415

S2 The local spin analysis

In a dimer system with two molecules A and B, the expectation value of spin-square operator $\langle \hat{S}^2 \rangle$ can be expressed as a sum of one and two-body contributions towards the total spin[6],

$$\left\langle \hat{S}^2 \right\rangle = \sum_A \left\langle \hat{S}_A^2 \right\rangle + \sum_{A,B\neq B} \left\langle \hat{S}_{AB}^2 \right\rangle \tag{1}$$

Here, the first term $\left\langle \hat{S}_A^2 \right\rangle$ accounts for the local spin contribution from the electron population of molecular A, and the second term $\left\langle \hat{S}_{AB}^2 \right\rangle = \left\langle \hat{S}_A \cdot \hat{S}_B \right\rangle$ adds the inter-molecular spin couplings. We construct a local spin density matrix with both one and two-particle wavefunctions to accurately account for the multiexcitonic transitions in the SF process.

$$\rho_{rs\in A} = \frac{1}{2S+1}(2.0 - 0.5N)\left[\gamma_{rs}^A - \sum_p \Gamma_{rpsp}^A\right] \tag{2}$$

where γ^A and Γ^A represent the one- and two-particle density matrices projected onto the localized orbital basis r, s of the molecule A, respectively. S is the spin multiplicity and N is the number of electrons (active electrons in DMRG calculations).

Using the local operator, it is natural to employ the decomposition scheme of the local spin distribution by Clark and Davidson. [7] We thus formulate the computation of the local spin square value in terms of the projected local density matrices,

$$\left\langle \hat{S}_A^2 \right\rangle = \frac{3}{4}\sum_r \gamma_{rr}^A - \frac{1}{2}\sum_{rs} \Gamma_{rsrs}^A - \frac{1}{4}\sum_{rs} \Gamma_{rssr}^A \tag{3}$$

For instance, the values of $\left\langle \hat{S}_A^2 \right\rangle$ for perfect singlet, doublet and triplet manifolds are 0.00, 0.75 and 2.00, respectively. The first term yields $\sum_r \gamma_{rr}^A = N_A$ that simply adds the spin square of each electron according to the number of electrons in molecule A, and the second term deals with the spin coupling between electrons within molecule A that modifies the additive contribution from the first term. This local spin formulation is rigorous, aside from the local fragment projector that can be defined in various ways which lead to different projected density matrices. For non-covalent pentacene dimer, the local fragment operator $\hat{P}(A)$ can be well defined using a subsystem projection that satisfies,

$$\sum_A \hat{P}(A) = \mathbf{I} \tag{4}$$

$$\hat{P}(A)\hat{P}(B) = \delta_{AB}\hat{P}(A) \tag{5}$$

Here we choose Pipek-Mezey localized active orbitals (ϕ_r) belonging to molecule A to build the projector,

$$\hat{P}(A) = \sum_{r\in A} |\phi_r\rangle\langle\phi_r| \tag{6}$$

One can also define a projector by removing the atomic components residing on other molecules according to

$$\hat{P}(A) = \left(\mathbf{1} - \sum_B \sum_{\mu\nu\in B} |\phi_\mu\rangle\, S_{\mu\nu}^{-\frac{1}{2}}\, \langle\phi_\nu|\right) \sum_{r\in A} |\phi_r\rangle\langle\phi_r| \tag{7}$$

But this loosely breaks the conditions in Eqs. (4) and (5). For non-covalent pentacene dimer, both forms of the local projection operator are found to yield similar local spin characters, as the projection of atomic components is only minor. Fig. S4 shows the 22 Pipek-Mezey localized orbitals employed in the local spin analysis. In all these orbitals, the electronic population is localized over one of the molecule in the dimer.

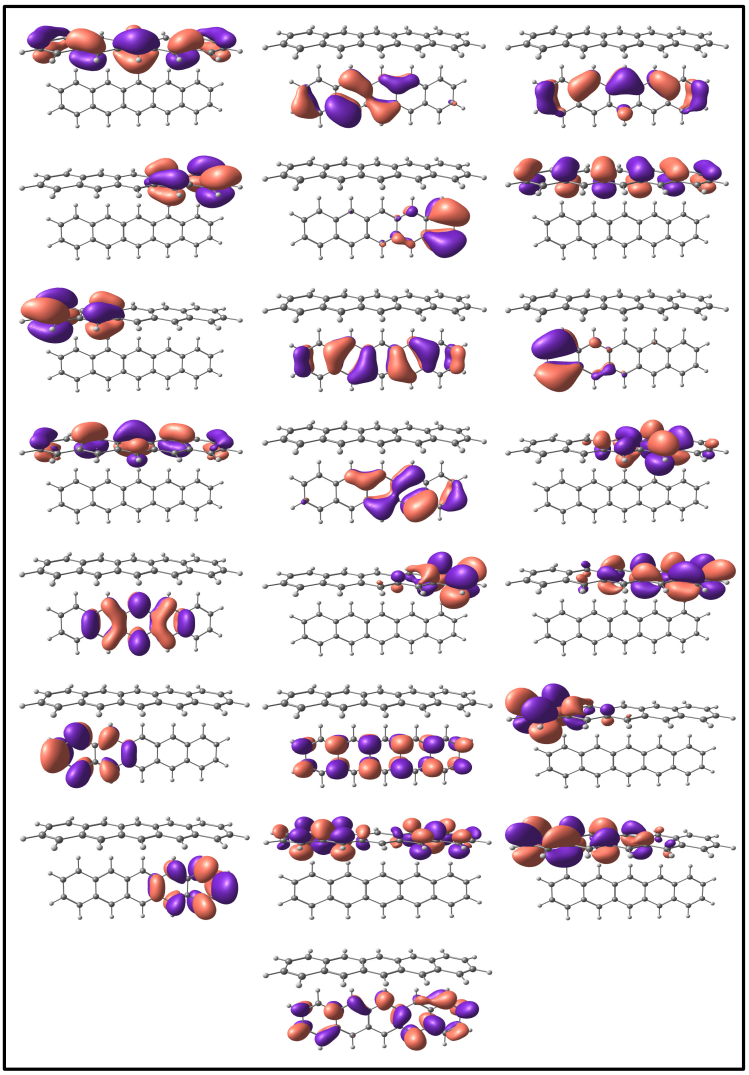

Fig. S4: The 22 Pipek-Mezey localized orbitals employed in the local spin analysis of pentacene dimer.

We have benchmarked our local spin analysis method to characterize the electronic states of few of the SF systems (DPBF and tetracene dimers) with the charge and spin analysis by Luzanov et al.[8] and obtained good agreement on the assignment of adiabatic state characters (Table S2 and S3).

Table S2: The characterization of electronic state for the dimer3 (A+D) structure of DPBF [Table VIII (Luzanov et al. J. Chem. Phys. 2015, 142, 224104).]

Luzanov et al.		Our work		
State	Character	State	Character	$\left\langle \hat{S}_A^2 \right\rangle$
^{1}ME	TT	S_1	TT	1.999
S_1	LE	S_2	LE	0.000
S_1'	LE	S_3	LE	0.000
S_2	CR	S_4	CT	0.750
S_2'	CR	S_5	CT	0.749

Table S3: The characterization of electronic state for the X-ray structure of tetracene dimer [Table IV (Luzanov et al. J. Chem. Phys. 2015, 142, 224104).]

Luzanov et al.		Our work		
State	Character	State	Character	$\left\langle \hat{S}_A^2 \right\rangle$
^{1}ME	TT	S_1	TT	1.902
S_1	LE	S_2	LE	0.051
S_1'	LE	S_3	LE	0.065
S_2	CR	S_4	CT	0.706
S_2'	CR	S_5	CT	0.766

S2.1 The natural transition orbitals

The nature of CT character in S_2 and S_4 states can be confirmed by visualizing the Natural Transition Orbitals (NTOs) for corresponding states obtained from DMRG calculations. Generally, the NTO analysis is performed for a CIS wavefunctions, where the sum of the square of each NTO singular value $\sum_i {\lambda_i}^2$ is exactly 1.[9] However, if the state of interest is not pure singlet state (like the DMRG many body wavefunction), $\sum_i {\lambda_i}^2$ would not be 1. The orbital distribution in the corresponding highest occupied and lowest unoccupied NTO pair is shown in Fig. S5

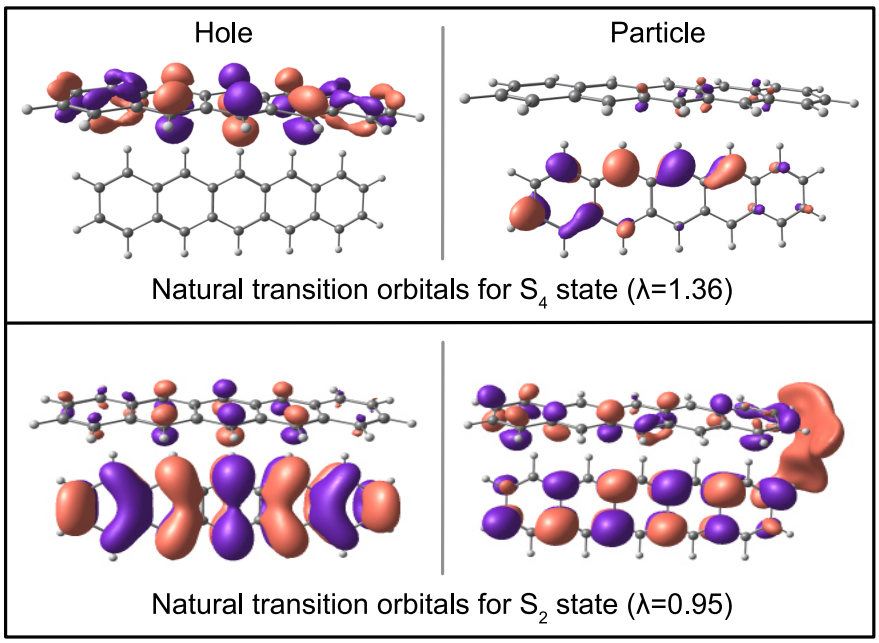

Fig. S5: The most significant natural transitions orbital pairs for the $S_0 \rightarrow S_4$ and $S_0 \rightarrow S_2$ transition in pentacene dimer at ISO value of $\pm 4 \times 10^{-2}$ a.u.

S3 The multipolar electronic interaction

Here we assume that the intermolecular Coulomb operator $\hat{V}_{\text{coul}}$ is well defined on the active orbitals that are well localized on the respective monomer molecule of the non-covalent dimer. For less critical divergence, we construct an intermolecular electronic interaction $H^{ele}_{mn} = \langle \Psi_m | \hat{V}_{\text{coul}} | \Psi_n \rangle$ based on the distributed many-center multipolar (dipole, quadrupole, hexapole and octupole) moments of $\hat{V}_{\text{coul}}$[10] between SF adiabatic states m and n. In the dimer system, where A and B represent the two molecules, the electronic interaction operator $H^{IJ,ele}_{mn}$ between the atom sites $I \in A$ and $J \in B$ can be defined in a many-center expansion, assuming the summation on the common Cartesian indices $(\alpha, \beta, \cdots)$,

$$\begin{aligned} H^{IJ,ele}_{mn} = & -T^{IJ}_{\alpha\beta}\mu^{I,mn}_{\alpha}\mu^{J,mn}_{\beta} - \frac{1}{3}T^{IJ}_{\alpha\beta\gamma}\left(\mu^{I,mn}_{\alpha}\Theta^{J,mn}_{\beta\gamma} - \Theta^{I,mn}_{\alpha\beta}\mu^{J,mn}_{\gamma}\right) \\ & - T^{IJ}_{\alpha\beta\gamma\delta}\left(\frac{1}{15}\mu^{I,mn}_{\alpha}\Omega^{J,mn}_{\beta\gamma\delta} - \frac{1}{9}\Theta^{I,mn}_{\alpha\beta}\mu^{J,mn}_{\gamma\delta} + \frac{1}{15}\hat{\Omega}^{I,mn}_{\alpha\beta\gamma}\mu^{J,mn}_{\delta}\right) \\ & - T^{IJ}_{\alpha\beta\gamma\delta\epsilon}\left(\frac{1}{105}\mu^{I,mn}_{\alpha}\Xi^{J,mn}_{\beta\gamma\delta\epsilon} - \frac{1}{45}\Theta^{I,mn}_{\alpha\beta}\Omega^{J,mn}_{\gamma\delta\epsilon} + \frac{1}{45}\hat{\Omega}^{I,mn}_{\alpha\beta\gamma}\Theta^{J,mn}_{\delta\epsilon} - \frac{1}{105}\Xi^{I,mn}_{\alpha\beta\gamma\delta}\mu^{J,mn}_{\epsilon}\right) \end{aligned} \tag{8}$$

where $T^{IJ}_{\alpha\beta\ldots v} = \frac{1}{4\pi\epsilon_0}\nabla_\alpha\nabla_\beta\ldots\nabla_v\frac{1}{\mathbf{R}_{IJ}}$ and $\mathbf{R}_{IJ}$ is the position vector between the atomic centers of two monomers (A and B). The lowest order contribution arises from the transition dipole-dipole interaction, since the transition charges are always zero as the transition density matrix is traceless due to the orthogonality of the ground and excited state adiabatic wavefunctions. The intermolecular Coulombic interaction between uncorrelated core electrons are easily computed at the Hartree-Fock level. The overall interaction between two molecules is evaluated as

$$H^{ele}_{mn} = \sum_{I\in A}\sum_{J\in B} H^{IJ,ele}_{mn} \tag{9}$$

The partitioning of distributed multipolar moments on two molecules can be based on the basis of atomic orbitals $(\mu, \nu, \cdots)$. When the transition multipoles are relocated with respect to the distributed origin $\mathbf{R}_I$ of the atom I belonging to the molecule M $(M = A, B)$, the explicit expressions for the transition dipole ($\mu_\alpha^{I,mn}$), quadrupole ($\mathbf{\Theta}_{\alpha\beta}^{I,mn}$), hexapole ($\mathbf{\Omega}_{\alpha\beta\gamma}^{I,mn}$) and octupole ($\mathbf{\Xi}_{\alpha\beta\gamma\delta}^{I,mn}$) moment tensors[11] between two SF electronic states m and n are given as,

$$\mu^{I,mn} = \sum_{\mu\nu\in I} \tau_{mn}^{\mu\nu} \left[\langle\mu|\nu\rangle \mathbf{R}_I - \langle\mu|\mathbf{r}|\nu\rangle\right] \tag{10}$$

$$\mathbf{\Theta}^{I,mn} = \sum_{\mu\nu\in I} \tau_{mn}^{\mu\nu} \left[-\mathbf{R}_I \otimes \mathbf{R}_I \langle\mu|\nu\rangle + \langle\mu|\mathbf{r}|\nu\rangle \otimes \mathbf{R}_I - \langle\mu|\mathbf{r}\otimes\mathbf{r}|\nu\rangle\right] \tag{11}$$

$$\begin{aligned}\mathbf{\Omega}^{I,mn} = \sum_{\mu\nu\in I} \tau_{mn}^{\mu\nu} \big[&\mathbf{R}_I \otimes \mathbf{R}_I \otimes \mathbf{R}_I \langle\mu|\nu\rangle - \mathbf{R}_I \otimes \mathbf{R}_I \otimes \langle\mu|\mathbf{r}|\nu\rangle - \mathbf{R}_I \otimes \langle\mu|\mathbf{r}|\nu\rangle \otimes \mathbf{R}_I - \langle\mu|\mathbf{r}|\nu\rangle \otimes \mathbf{R}_I \otimes \mathbf{R}_I \\ &+\mathbf{R}_I \otimes \langle\mu|\mathbf{r}\otimes\mathbf{r}|\nu\rangle + \langle\mu|\mathbf{r}\otimes\mathbf{R}_I\otimes\mathbf{r}|\nu\rangle + \langle\mu|\mathbf{r}\otimes\mathbf{r}|\nu\rangle \otimes \mathbf{R}_I - \langle\mu|\mathbf{r}\otimes\mathbf{r}\otimes\mathbf{r}|\nu\rangle\big]\end{aligned} \tag{12}$$

$$\begin{aligned}\mathbf{\Xi}^{I,mn} = \sum_{\mu\nu\in I} \tau_{mn}^{\mu\nu} \big[&-\mathbf{R}_I \otimes \mathbf{R}_I \otimes \mathbf{R}_I \otimes \mathbf{R}_I \langle\mu|\nu\rangle + \mathbf{R}_I \otimes \mathbf{R}_I \otimes \mathbf{R}_I \otimes \langle\mu|\mathbf{r}|\nu\rangle + \mathbf{R}_I \otimes \mathbf{R}_I \otimes \langle\mu|\mathbf{r}|\nu\rangle \otimes \mathbf{R}_I \\ &+\mathbf{R}_I \otimes \langle\mu|\mathbf{r}|\nu\rangle \otimes \mathbf{R}_I \otimes \mathbf{R}_I + \langle\mu|\mathbf{r}|\nu\rangle \otimes \mathbf{R}_I \otimes \mathbf{R}_I \otimes \mathbf{R}_I - \mathbf{R}_I \otimes \mathbf{R}_I \otimes \langle\mu|\mathbf{r}\otimes\mathbf{r}|\nu\rangle \\ &-\mathbf{R}_I \otimes \langle\mu|\mathbf{r}\otimes\mathbf{r}|\nu\rangle \otimes \mathbf{R}_I - \langle\mu|\mathbf{r}\otimes\mathbf{r}|\nu\rangle \otimes \mathbf{R}_I \otimes \mathbf{R}_I + \mathbf{R}_I \otimes \langle\mu|\mathbf{r}\otimes\mathbf{r}\otimes\mathbf{r}|\nu\rangle \\ &+\langle\mu|\mathbf{r}\otimes\mathbf{r}\otimes\mathbf{r}|\nu\rangle \otimes \mathbf{R}_I - \mathbf{R}_I \otimes \langle\mu|\mathbf{r}\otimes\mathbf{R}_I\otimes\mathbf{r}|\nu\rangle - \langle\mu|\mathbf{r}\otimes\mathbf{R}_I\otimes\mathbf{r}|\nu\rangle \otimes \mathbf{R}_I - \langle\mu|\mathbf{r}\otimes\mathbf{r}\otimes\mathbf{r}\otimes\mathbf{r}|\nu\rangle \\ &+\langle\mu|\mathbf{r}\otimes\mathbf{R}_I\otimes\mathbf{r}\otimes\mathbf{r}|\nu\rangle + \langle\mu|\mathbf{r}\otimes\mathbf{r}\otimes\mathbf{R}_I\otimes\mathbf{r}|\nu\rangle - \langle\mu|\mathbf{r}\otimes\mathbf{R}_I\otimes\mathbf{R}_I\otimes\mathbf{r}|\nu\rangle\big]\end{aligned} \tag{13}$$

where $\tau_{mn}^{\mu\nu}$ is the DMRG transition density matrix between two excited states m and n, and the outer products $(\otimes)$ are carried out between two vectors.

S4 The theory of vibronic coupling analysis

We consider a vibronic Hamiltonian H_{mn}^{vib} expanded as a Taylor series around the equilibrium position $\mathbf{Q}$=0 of the ground state of pentacene dimer[12],

$$H_{mn}^{vib}(\mathbf{Q}) = H_{mn}(\mathbf{0}) + \sum_i Q_i \frac{\partial H_{mn}(\mathbf{Q})}{\partial Q_i}\bigg|_{\mathbf{Q}=\mathbf{0}} + \sum_{ij} Q_i Q_j \frac{\partial^2 H_{mn}(\mathbf{Q})}{\partial Q_i \partial Q_j}\bigg|_{\mathbf{Q}=\mathbf{0}} + \ldots \tag{14}$$

where m and n are any two SF adiabatic states in this context. i and j are two vibrational modes for the dimer. The zeroth order term in eq. (9) represents the *ab-initio* DMRG electronic energies and the first term relates to the first-order vibronic couplings. Higher order vibronic couplings are not included in this study. Tokunaga and Sato[13,14] proposed the calculation of VCs in terms of Holstein (intrastate) and Peierls (interstate) couplings as a function of spatial wavefunctions. We incorporated DMRG based spatial state and transition densities to analyze these interactions in pentacene dimer,

$$\begin{aligned}\frac{\partial H_{nn}(\mathbf{Q})}{\partial Q_i}\bigg|_{\mathbf{Q}=\mathbf{0}} &= \int \mathrm{d}\mathbf{r} \bar{\gamma}_n^{\mathrm{diff}}(\mathbf{r}) v_i(\mathbf{r}) \\ \frac{\partial H_{mn}(\mathbf{Q})}{\partial Q_i}\bigg|_{\mathbf{Q}=\mathbf{0}} &= \int \mathrm{d}\mathbf{r} \bar{\tau}_{mn}^{\mathrm{tra}}(\mathbf{r}) v_i(\mathbf{r})\end{aligned} \tag{15}$$

where, $\bar{\gamma}_n^{\mathrm{diff}}(\mathbf{r})$ represents the DMRG difference density between an excited state(n) and the ground state(0).

$$\bar{\gamma}_n^{\mathrm{diff}}(\mathbf{r}) = \bar{\gamma}_n(\mathbf{r}) - \bar{\gamma}_0(\mathbf{r}) \tag{16}$$

The vibronic coupling density η for a vibrational mode i is defined to analyze the vibronic couplings. For example, the Holstein coupling density is calculated as,

$$\eta_i(\mathbf{r}) = \bar{\gamma}_n^{\mathrm{diff}}(\mathbf{r}) v_i(\mathbf{r}) \tag{17}$$

The $\bar{\gamma}_n$ and the $\bar{\tau}_{mn}^{\mathrm{tra}}$ are the electronic density of a state n and the transition density between two states m and n, respectively. v_i is the potential derivative defined as,

$$v_i(\mathbf{r}) = \sum_I^{N_{\mathrm{atom}}} \left(\frac{\partial}{\partial Q_i} \frac{-Z_I}{|\mathbf{r} - \mathbf{R}_I|} \right) \Bigg|_{\mathbf{Q}=0} \tag{18}$$

The vibrational coordinate Q_i relates to a dimensionless normal coordinate q_i at a frequency ω_i such as,

$$Q_i = \sqrt{\frac{\hbar}{\omega_i}} q_i \tag{19}$$

The vibrational coordinate Q_i can be projected to 3N Cartesian coordinates by,

$$R_\beta = \frac{1}{\sqrt{M_\beta}} \sum_{i=1}^{3N-6} L_{\beta i} Q_i \quad (\beta = 1, 2, \ldots, 3N) \tag{20}$$

where M_β denotes the nuclear mass associated with its position at R_β, and $L_{\beta i}$ forms the transformation matrix from normal to Cartesian coordinates obtained from vibrational analysis.

The difference and transition densities are related to the density matrices represented in the DMRG active orbitals, respectively, as follows,

$$\bar{\gamma}_n^{\mathrm{diff}}(\mathbf{r}) = \sum_{pq} \gamma_{n,pq}^{\mathrm{diff}} \phi_p^*(\mathbf{r}) \phi_q(\mathbf{r}), \tag{21}$$

$$\bar{\tau}_{mn}^{\mathrm{tra}}(\mathbf{r}) = \sum_{pq} \tau_{mn,pq}^{\mathrm{tra}} \phi_p^*(\mathbf{r}) \phi_q(\mathbf{r}). \tag{22}$$

In our implementation, the Holstein (Peierls) couplings of Eqs. (15) are computed by tracing the product of the difference (transition) density matrix and the derivative potential matrix represented in the active orbital basis,

$$\frac{\partial H_{nn}(\mathbf{Q})}{\partial Q_i}|_{\mathbf{Q}=\mathbf{0}} = \mathrm{tr}\Big\{ \gamma_n^{\mathrm{diff}} \mathbf{v}_i \Big\} \tag{23}$$

$$\frac{\partial H_{mn}(\mathbf{Q})}{\partial Q_i}|_{\mathbf{Q}=\mathbf{0}} = \mathrm{tr}\big\{ \tau_{mn}^{\mathrm{tra}} \mathbf{v}_i \big\}. \tag{24}$$

Next, we show how the derivative potential matrix $\mathbf{v}_i$ for each Q_i mode is evaluated. The matrix element $v_{i,pq}$ is given as

$$\begin{aligned} v_{i,pq} &= \sum_I^{N_{\mathrm{atom}}} \langle \phi_p | \frac{\partial}{\partial Q_i} \frac{-Z_I}{|\mathbf{r} - \mathbf{R}_I|} | \phi_q \rangle \\ &= \sum_I^{N_{\mathrm{atom}}} \langle \phi_p | \frac{\partial}{\partial \mathbf{R}_I} \frac{-Z_I}{|\mathbf{r} - \mathbf{R}_I|} | \phi_q \rangle \frac{\partial \mathbf{R}_I}{\partial Q_i} \\ &= \sum_I^{N_{\mathrm{atom}}} c_{\mu p}^* c_{\nu q} \langle \phi_\mu | \frac{\partial}{\partial \mathbf{r}} \frac{Z_I}{|\mathbf{r} - \mathbf{R}_I|} | \phi_\nu \rangle \frac{\partial \mathbf{R}_I}{\partial Q_i}. \end{aligned} \tag{25}$$

In the last equation, the transformations are made from atomic orbitals ϕ_μ and ϕ_ν using the orbital coefficients $c_{\mu p}$ and $c_{\nu q}$, respectively. By further noting the relation

$$\frac{\partial}{\partial \mathbf{r}} \langle \phi_\mu | \frac{Z_I}{|\mathbf{r} - \mathbf{R}_I|} | \phi_\nu \rangle = 0, \tag{26}$$

the derivative potential is formulated in terms of the analytical first-derivative integrals that are readily computed in our program,

$$v_{i,pq} = - \sum_{I}^{N_{\text{atom}}} c^*_{\mu p} c_{\nu q} \left[\left\langle \frac{\partial}{\partial \mathbf{r}} \phi_\mu \middle| \frac{Z_I}{|\mathbf{r} - \mathbf{R}_I|} \middle| \phi_\nu \right\rangle + \left\langle \phi_\mu \middle| \frac{Z_I}{|\mathbf{r} - \mathbf{R}_I|} \middle| \frac{\partial}{\partial \mathbf{r}} \phi_\nu \right\rangle \right] \frac{\partial \mathbf{R}_I}{\partial Q_i} \tag{27}$$

S5 The microscopic origin of vibronic couplings

The first-order vibronic couplings can be separated into two parts: (i) intrastate or interstate couplings based on the difference and transition densities, respectively and (ii) the potential derivative v_i. A vibronic coupling density (VCD) analysis is performed to understand the origin of VCs from an interaction between electronic and vibrational structures.

To address the question about the microscopic origin of these couplings due to vibronic modulation, the VCD analysis leads to the visualization the HC and PCs in real space. Fig. S6(a-d) shows the difference densities of S_1, S_2, S_3 and S_4 states, respectively. The transition densities for $S_1 \rightarrow S_2$, $S_1 \rightarrow S_3$, $S_3 \rightarrow S_4$ and $S_1 \rightarrow S_4$ transitions, relating to corresponding PCs are shown in Fig. S6(e-h). The product of these difference (transition) densities with the potential derivative for a vibrational mode is used to calculate the corresponding HC (PC).[13] The difference density sketches the spatial distribution of the difference between the molecular orbital densities of the states involved in the transition, however the transition density represents a spatial map of a product of these molecular orbital densities.

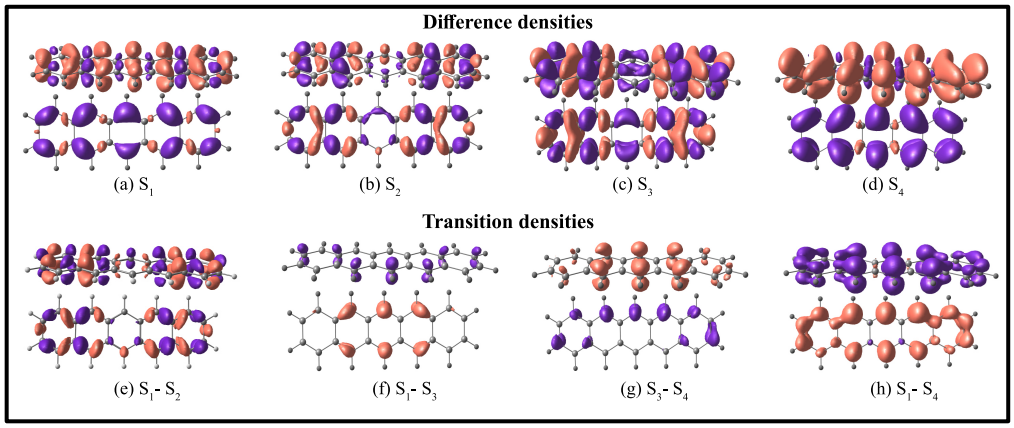

Fig. S6: The DMRG difference densities (a-d) and transition densities (e-h) for low-lying excited states and the transitions in pentacene dimer. The blue and orange surfaces represent the positive and negative isosurfaces at ISO value of $\pm 5 \times 10^{-4}$ a.u.).

The difference density for S_1 shows both positive and negative distribution in the two molecules due to the multiexcitonic nature of the state, with more negative distribution at C=C bonds in the upper molecule which can be attributed to the $\pi \rightarrow \pi^*$ nature of the transition (Fig. S6(a)). Fig. S6(b) depicts the presence of the weak CT character in S_2 state as there is only a slight

difference between the density distribution in upper and lower molecule. The difference density for S_3 states have equal but both positive and negative distribution in both molecules, confirming the fact that this transition involves a local character (Fig. S6(c)). For the S_4 state, the difference density primarily has positive and negative distributions in the upper and lower part of the molecule, reiterating that this state has a strong CT character (Fig. S6(d)). The vibrational vectors for the C=C stretching mode at 1615^i cm^{-1} are uniformly distributed throughout the pentacene unit (ABCBA), with the ring 'C' being static (Fig. S11(i)). This vibration overlaps well with the difference density in the 'AB/BA' region and induces a vibronic density of 215 meV in the molecule which is distributed throughout the dimer skeleton with more population at the side (A) part of the pentacene dimer, as large displacement vectors for vibration are observed in this region (Fig. S7(a)). In the similar regions, an 'out-of-phase' normal mode at 1615^o cm^{-1} (Fig. S11(j)) induces a strong HC of 452 meV in the molecule (Fig. S7(c)). Some low-frequency vibrations such as out-of-phase ring bending mode at 101^o cm^{-1} (Fig. S11(b)) also induces a strong HC of 356 meV in the S_4 state (Fig. S7(b)). Such long-range interactions easily get activated by thermal excitation and have the potential to significantly oscillate the energy of the CT states.

To analyze the origin of PCs, the transition densities are plotted in Fig. S6(e-h) for different transitions. The equally distributed transition density in both $S_1 \rightarrow S_3$ and $S_3 \rightarrow S_4$ represents that both the 'TT$\rightarrow$ LE' and 'LE$\rightarrow$ CT2' are charge-transfer transitions or must occur through a CT mediated state. A similar but strong transition density for $S_1 \rightarrow S_4$ transition validates the strong CT based interaction between these two states as predicted by local spin distribution. The ring breathing mode at 778^o cm^{-1} (Fig. S11(e)) gives rise to a VCD of 148 meV in the middle region of the lower molecule owing to the fact that the transition density, as well as the vibrational vectors are localized in this region (Fig. S7(d)). On the other hand the in-phase vibration at 1332^i cm^{-1} (Fig. S11(h)) is widely distributed in the molecule, causing a relatively weak PC of 74 meV for $S_3 \rightarrow S_4$ transition (Fig. S7(e)). Similarly, the $S_1 \rightarrow S_4$ transition for C=C stretching mode at 1204^o cm^{-1} (Fig. S11(g)) shows a strong PC of 459 meV in the intermolecular region between the molecules, primarily located near the upper molecule as the vibrational motion in the lower fragment affects the distribution of potential derivative in the upper regions, differently (Fig. S7(f)).

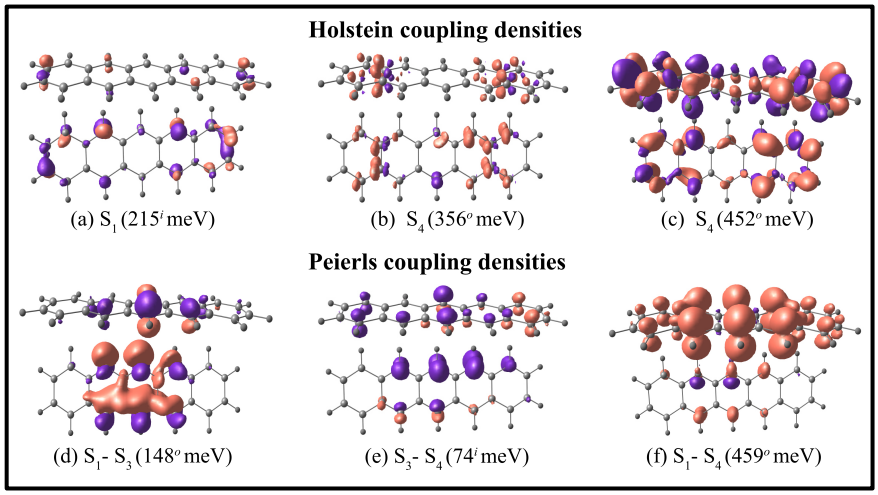

Fig. S7: Vibronic coupling densities: The Holstein [for normal mode at 1615^i cm^{-1} (a) 101^o cm^{-1} (b) and 1615^o cm^{-1} (c)]; and Peierls [for normal mode at 778^o cm^{-1} (d), 1332^i cm^{-1} (e) and 1204^o cm^{-1} (f)] coupling densities (ISO value: $\pm 5 \times 10^{-5}$ a.u.).

A possible way to include these VCs in explaining the mechanism of SF can be understood by a bath engineering point of view based on e-ph interaction. As well known, a phonon creation

and annihilation induce the addition and subtraction of the energy quanta to the bath, during the process of electronic transition or the oscillation of electronic states. To consider the energy conservation, it is desirable that the adiabatic energy should match with the corresponding vibrational frequency for an efficient SF. For our dimer, we identify several modes with significant HCs such as - 114 meV at 1615^{i} cm^{-1} for S_2, 126 meV at 1716^{o} cm^{-1} for S_3 and 258 meV at 1615^{o} cm^{-1} for S_4 states. Interestingly, these couplings correspond to the energy gap of these states with S_1, which is 0.08, 0.14 and 0.31 eV for S_2, S_3 and S_4 states, respectively. The PCs can also provide such energy matching to facilitate efficient SF as depicted in Fig. S7(d-e). Actually, it can be estimated that there are several multimode pathways activated within the molecule which help in populating the S_1 state through multistate vibronic interaction, so that it can be a multiexcitonic state in the true sense.

The other important HCs and PCs are plotted in Figure S8 and Figure S9, respectively with the all related vibrational vectors shown in Figure S11.

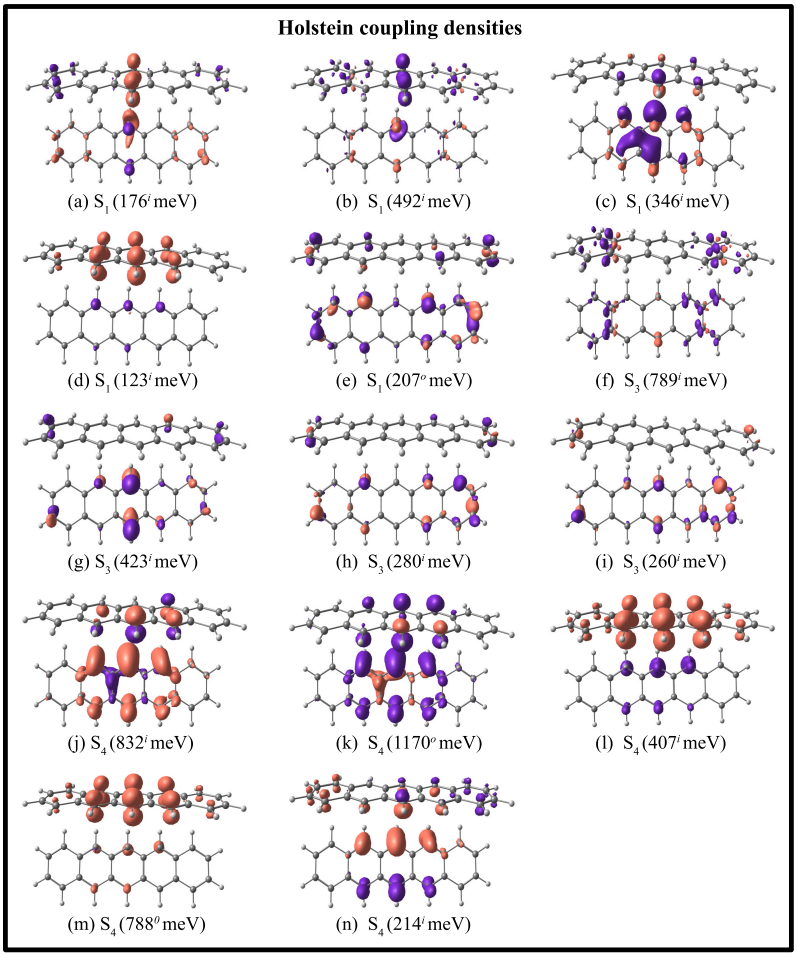

Fig. S8: Other significant Holstein coupling densities for SF states in pentacene dimer at (a) 101^{i} (b) 476^{i} (c) 778^{i} (d) 1204^{i} (e) 1615^{o} (f) 476^{i} (g) 726^{i} (h) 1615^{i} (i) 1716^{i} (j) 778^{i} (k) $778\ ^{o}$ (l) 1204^{i} (m) 1204^{o} (n) 1332^{i} cm^{-1}. The in-phase and out-of-phase vibrations are distinguished with the subscripts 'i' and 'o', respectively.

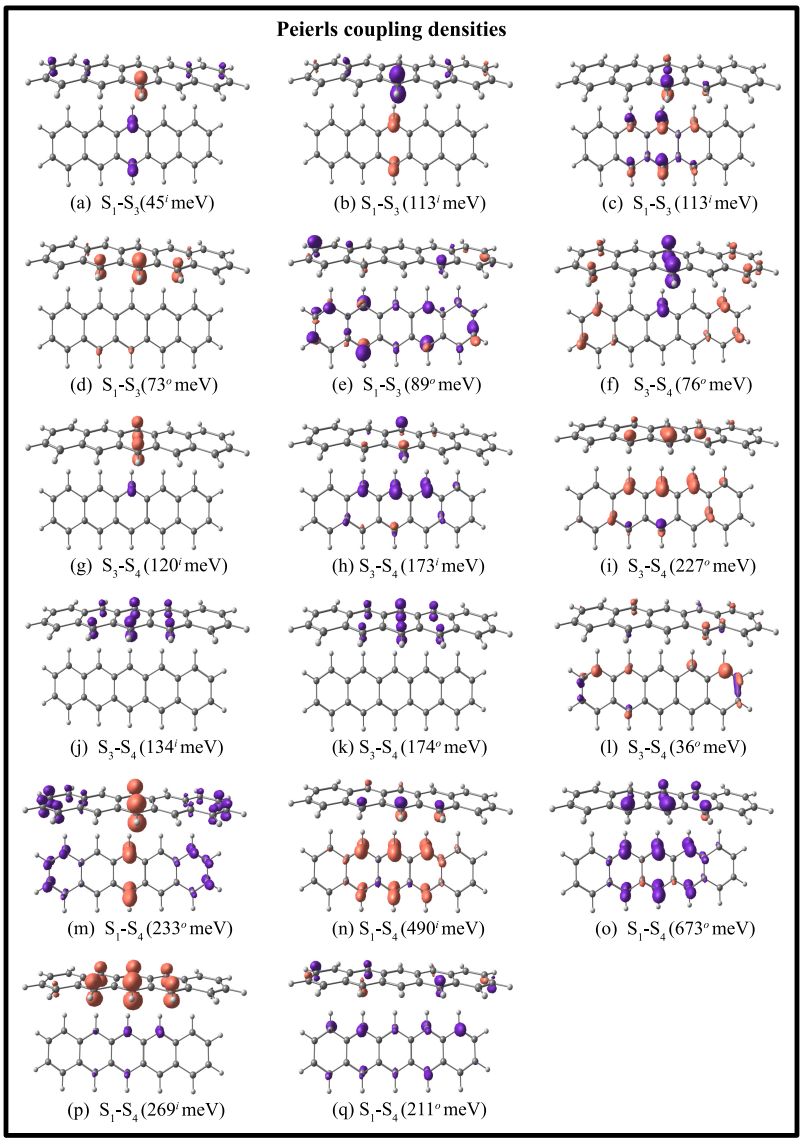

Fig. S9: Other significant Peierls coupling densities for SF states in pentacene dimer at (a) 101^i (b) 476^i (c) 778^i (d) 1204^o (e) 1615^o (f) 101^o (g) 476^i (h) 778^i (i) 778^o (j) 1204^i (k) $1204\ ^o$ (l) 1615^o (m) 101^o (n) 778^i (o) 778^o (p) 1204^i (q) 1615^o cm^{-1}. The in-phase and out-of-phase vibrations are distinguished with the subscripts 'i' and 'o', respectively.

S5.1 The superposition of normal modes

In calculating the vibronic couplings in the dimer, we considered two ways to superimpose the vibrational motion of monomer (i) in-phase and (ii) out-of-phase. The normal modes of dimer are examined to be the linear combination of that of the monomers. During in-phase motion, the atoms in both fragments reach their respective maximum positive (negative) vibrational displacement at the same time. However, the atoms in different fragments vibrate in opposite vibrational directions during the out-of-phase motion. The in-phase and out-of-phase vibrations are distinguished with the subscripts 'i' and 'o', respectively.

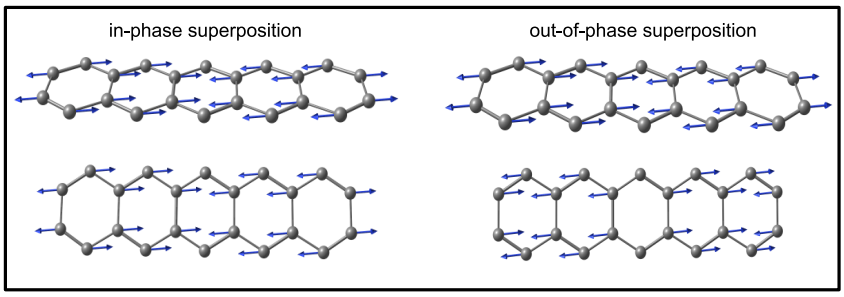

Fig. S10: The example of in-phase and out-of-phase superposition of monomer vibrational modes (101 cm^{-1}) into a dimer. The H-atoms in the molecule are omitted.

Table S4: Comparison of dimer and monomer normal mode symmetries. The totally symmetric vibrations do not change the center of the molecule.

Modes	dimer in-phase	dimer out-of-phase
monomer symmetric	Symmetric	Symmetric
monomer asymmetric	Asymmetric	Symmetric

S5.2 Normal vibrational modes of pentacene dimer

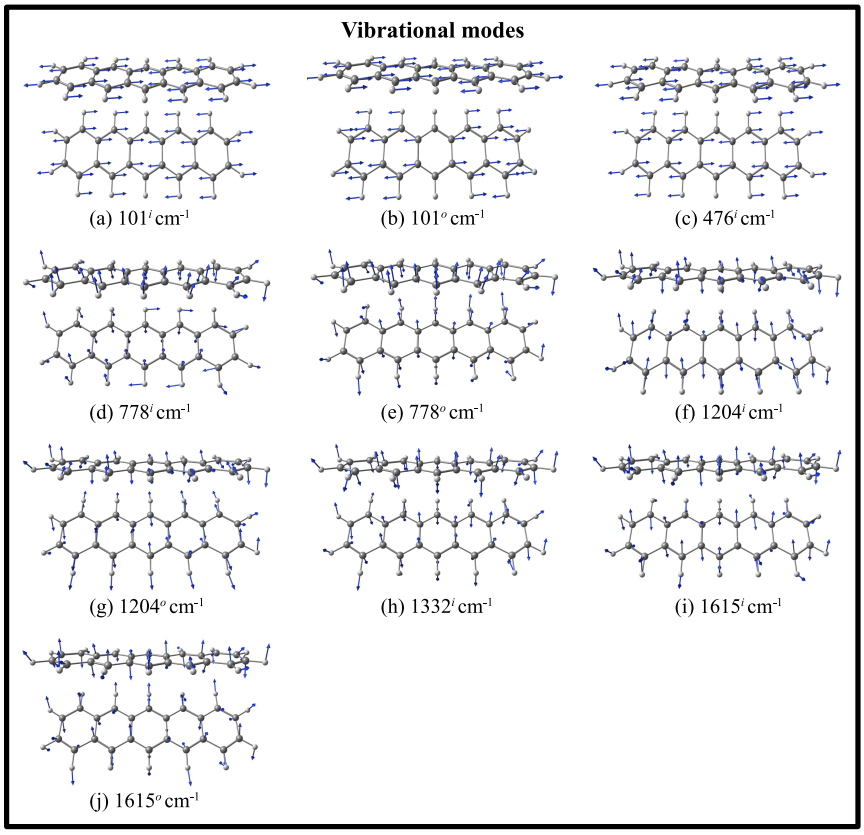

Fig. S11: Normal vibrational modes of pentacene dimer.

S6 A multistate Holstein-Peierls Hamiltonian

We consider the vibronic wavefunction ($\Psi(\mathbf{r},\mathbf{Q})$ for S'_m) in the expansion of the adiabatic SF eigenstates ($\psi_n(\mathbf{r};\mathbf{0})$ for S_n) obtained from the reference electronic Hamiltonian $\hat{H}_e(\mathbf{r};\mathbf{0})$,

$$\Psi(\mathbf{r},\mathbf{Q}) = \sum_n \chi_n(\mathbf{Q})\psi_n(\mathbf{r};\mathbf{0}) \tag{28}$$

$$\hat{H}_e(\mathbf{r};\mathbf{0})\psi_n(\mathbf{r};\mathbf{0}) = E_n(\mathbf{0})\psi_n(\mathbf{r};\mathbf{0}) \tag{29}$$

The resulting vibronic wavefunction is exact if all adiabatic eigenstates are used as the basis states. Here we assume that low-lying vibronic states are well approximated by the six adiabatic SF states of pentacene dimer that exhibit a range of characters. Given the linear vibronic coupling elements $\frac{\partial H_{nn}(\mathbf{Q})}{\partial Q_i}$ (Holstein coupling) and $\frac{\partial H_{mn}(\mathbf{Q})}{\partial Q_i}$ (Peierls coupling for $m \neq n$) in terms of the normal mode displacements Q_i, the Holstein-Peierls vibronic model Hamiltonian takes the form in the adiabatic basis states,

$$\hat{H}(\mathbf{r},\mathbf{Q}) = \sum_n |\psi_n\rangle\, H_{nn}(\mathbf{0})\, \langle\psi_n| + \sum_n |\psi_n\rangle \sum_i Q_i \frac{\partial H_{nn}(\mathbf{Q})}{\partial Q_i} \langle\psi_n| + \sum_{m\neq n} |\psi_m\rangle \sum_i Q_i \frac{\partial H_{mn}(\mathbf{Q})}{\partial Q_i} \langle\psi_n| \tag{30}$$

where the static Hamiltonian is

$$H_{nn}(\mathbf{0}) = E_n(\mathbf{0}) + \sum_i \frac{1}{2}\omega_i \left(-\frac{\partial^2}{\partial Q_i^2} + Q_i^2\right) \tag{31}$$

Further, $\hat{H}(\mathbf{r},\mathbf{Q})$ is diagonalized to obtain χ_n for determining the vibronic state Ψ_m along with the cumulative vibrational coordinates as the normal mode displacements $\mathbf{Q}$ (approximated in the in-phase and out-of-phase linear combination of the monomer modes). It is obvious that only totally symmetric modes can make nonzero contributions to Holstein coupling but are unimportant to Peierls couplings (between two states of different characters). The analysis of the dimer mode symmetry is given in Table S4.

In our calculations, however, the adiabatic states S_n and the vibrational modes Q_i are computed using different structures: the adiabatic S_n and the energies E_n are computed using the dimer that is built by combining the CASSCF optimized monomer geometry, while the normal modes are computed using the dimer that is built by combining the DFT optimized monomer geometry. There is an obvious discrepancy between the DFT-based structure at which the Holstein-Peierls vibronic Hamiltonian is defined and the CASSCF-based structure at which the vibronic state is constructed. In other words, $\psi_n(\mathbf{r};\mathbf{0})$ no longer remain the eigenstate of $\hat{H}_e(\mathbf{r};\mathbf{0})$. To approximately circumvent this problem which inevitably affects the vibronic Hamiltonian, we add electron-electron and electron-nucleus Coulombic corrections $\delta H_{mn}(\mathbf{0})$ to Peierls element,

$$\hat{H}(\mathbf{r},\mathbf{Q}) \;\rightarrow\; \hat{H}(\mathbf{r},\mathbf{Q}) + \sum_{m\neq n} |\psi_m\rangle\, \delta H_{mn}(\mathbf{0})\, \langle\psi_n| \tag{32}$$

$$\delta H_{mn}(\mathbf{0}) \;=\; \delta V^{ee}_{mn}(\mathbf{0}) + \delta V^{en}_{mn}(\mathbf{0}), \tag{33}$$

while still remaining DMRG/NEVPT2 E_n on the diagonal Holstein. The electron-electron correction δV^{ee}_{mn} can be computed using the many-center multipolar formula introduced in Section S3 by tracing the product of the DMRG transition density matrix τ_{mn} and the difference of multipoles between DFT and CASSCF geometries. The electron-nucleus correction δV^{en}_{mn} is simply computed as,

$$\delta V^{en}_{mn} = \mathrm{tr}\Big\{\hat{\tau}_{mn}\delta\hat{V}_{en}\Big\} \tag{34}$$

with $\delta\hat{V}_{en} = -\sum_I Z_I \left(\frac{1}{|\mathbf{r}-\mathbf{R}_I^{\mathrm{DFT}}|} - \frac{1}{|\mathbf{r}-\mathbf{R}_I^{\mathrm{CASSCF}}|}\right)$ the electron-nucleus attractive potential.

S7 The e-ph couplings in pentacene crystal

The electron-phonon interaction in our study is described by the Fröhlich Hamiltonian, which is expressed as

$$\hat{H}^{ep} = \sum_{mn\mathbf{k}\nu\mathbf{q}} g_{mn\mathbf{k},\nu\mathbf{q}} \hat{c}^{\dagger}_{m\mathbf{k}+\mathbf{q}} \hat{c}_{n\mathbf{k}} (\hat{a}_{\mathbf{q}\nu} + \hat{a}^{\dagger}_{-\mathbf{q}\nu}) \tag{35}$$

where $\hat{a}^{\dagger}_{\mathbf{q}\nu}$ and $\hat{a}_{-\mathbf{q}\nu}$ denote the creation and annihilation operators for a phonon of the ν-th vibration mode with momentum $\mathbf{q}$, and $\hat{c}^{\dagger}_{n\mathbf{k}}$ and $\hat{c}_{n\mathbf{k}}$ denote the creation and annihilation operators for an electron in the n-th electronic state with momentum $\mathbf{k}$. The electron-phonon matrix element $g_{mn\mathbf{k},\nu\mathbf{q}}$ is in the following definition, the calculation of which is implemented in the Quantum Espresso codes.

$$g_{mn\mathbf{k},\nu\mathbf{q}} = \frac{1}{\sqrt{2\omega_{\nu\mathbf{q}}}} \langle \psi_{m\mathbf{k}+\mathbf{q}}(\mathbf{r}) | \partial_{\nu\mathbf{q}} V(\mathbf{r}) | \psi_{n\mathbf{k}}(\mathbf{r}) \rangle \tag{36}$$

The probability of finding the initial state $|S_i\rangle$ in the final state $|S_f\rangle$ can be described by the $\mathcal{S}$-matrix theory.[15] We note that, for $n = 1$ term, it must vanish as it contains the unpaired creation or annihilation operators of phonon. To the lowest order of non-zero terms in $\mathcal{S}$-matrix terms, we should consider the transition matrix element for $n = 2$ as-

$$\begin{aligned} \langle S_f | (\hat{H}^{ep})^2 | S_i \rangle &= \sum_{vcv'c'\mathbf{k}\mathbf{k}'\mathbf{q}\mathbf{q}'} \langle 0 | A^{S_i}_{vc\mathbf{k}} A^{S_f\,*}_{v'c'\mathbf{k}'} \hat{c}^{\dagger}_{v'\mathbf{k}'} \hat{c}_{c'\mathbf{k}'} (\hat{H}^{ep})^2 \hat{c}^{\dagger}_{c\mathbf{k}} \hat{c}_{v\mathbf{k}} | 0 \rangle \\ &= \sum_{vcv'c'\nu\nu'\mathbf{k}\mathbf{q}} A^{S}_{vc\mathbf{k}} A^{S_f\,*}_{v'c'\mathbf{k}} g_{vv'\mathbf{k},\nu'\mathbf{q}} g_{cc'\mathbf{k},\nu\mathbf{q}} \end{aligned} \tag{37}$$

with the wavefunction of an excited state expressed as,

$$|S_i\rangle = \sum_{vc\mathbf{k}} A^{S_i}_{vc\mathbf{k}}\ \hat{c}^{\dagger}_{c\mathbf{k}} \hat{c}_{v\mathbf{k}} |0\rangle \tag{38}$$

where $|0\rangle$ represents the ground state and $A^{S_i}_{vc\mathbf{k}}$ are the coefficients of excited state obtained by solving Bethe-Salpeter equation (BSE), implemented in the BerkeleyGW codes.

Our calculations are based on density functional theory (DFT) and many-body perturbation theory, including the GW and BSE method. We first calculated the mean-field wavefunctions and eigenvalues based on the DFT, implemented in the Quantum Espresso package, within the local density approximation (LDA) functional.[16] The pseudopotential was used in a norm-conserving type with a energy cutoff 80 Ry. The force and electronic convergence tolerance is set to 0.01 eV Å^{-1} and 10^{-8} eV. A Monkhorst–Packcentered k grid is set to 7×7×7 in the structure optimization, while it is set to 11×11×11 in the self-consistent calculation. The phonon properties are obtained by diagonalizing the force constant matrix with density functional perturbation theory (DFPT).[17]

After diagonalization of $\hat{H}^{ep}$, the eigenvectors S'_x, where $x = 0, 1, \cdots, 5$, represent new SF electronic states which are a linear combination of SF basis states in pentacene crystal. As a result of e-ph interactions in the pentacene crystal, the S_1 state stabilizes (Table S5) and substantial mixing among electronic states are evident (Fig. S12).

Table S5: The final excited state energies (eV) in pentacene crystal [GW/BSE, in eV] modified as a result of e-ph interactions

State	Energy
S'_1	1.55
S'_2	1.78
S'_3	1.85
S'_4	1.96
S'_5	2.67

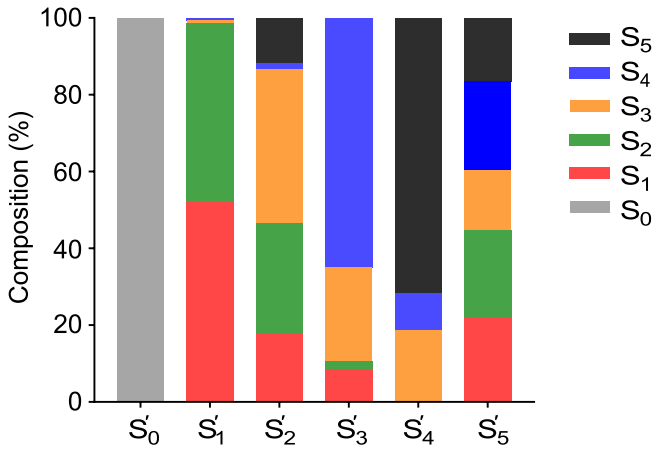

Fig. S12: The composition of final SF electronic states of pentacene crystal as a function of SF basis states.

S8 The exciton size

The charge-transfer number[9] Ω^{AB} is calculated by summing up the contributions to DMRG one-particle transition density matrix from individual molecules A and B in the dimer -

$$\Omega^{AB} = \frac{1}{2}\sum_{r\in A}\sum_{s\in B}\left[(\tau^{0n}\mathbf{S})_r(\mathbf{S}\tau^{0n})_{rs} + \tau^{0n}_{rs}(\mathbf{S}\tau^{0n}\mathbf{S})_r\right] \tag{39}$$

where $\mathbf{S}$ is the overlap matrix. An exciton size is determined by -

$$d_{exc} = \sqrt{\frac{1}{\Omega}\sum_{A,B}\Omega^{AB}(d^{AB})^2} \tag{40}$$

Here, Ω is a normalization factor computed by summing over Ω^{AB} and d^{AB} is the distance between the centers-of-mass of two molecules in the pentacene dimer.

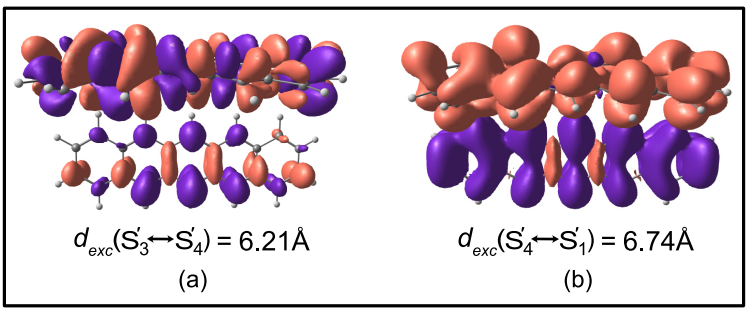

Fig. S13: A delocalization of transition densities over two molecules in pentacene dimer for $S^{\dagger}_3 \leftrightarrow S^{\dagger}_4$ (a) and $S^{\dagger}_4 \leftrightarrow S^{\dagger}_1$ (b) transitions caused by out-of-phase vibronic modulations at **Q**=0.10 in the vibronic stretching region.

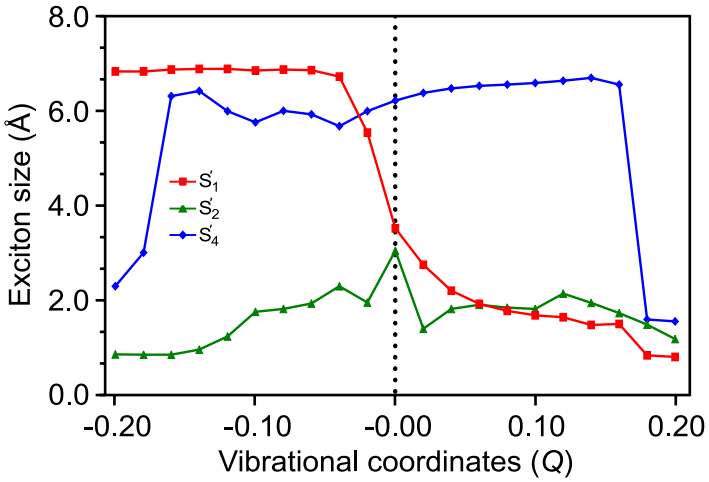

Fig. S14: The exciton sizes for SF states along with the in-phase vibronic modulations.

S9 Coordinates

1. The Cartesian coordinates of pentacene monomer (in Å) optimized for the ground (S_0) state at M062X/cc-pVTZ level of theory with E(S_0)=-846.7252490 E_h.

C	1.28320100	-0.48314700	-0.11606800	C	-1.31043000	0.54737800	0.12254100
C	0.77507900	-0.21099300	1.15285200	C	-0.80230900	0.27522600	-1.14633900
C	1.52588100	-0.43778900	2.32601900	C	-1.55311500	0.50202100	-2.31954400
C	1.01621000	-0.16609400	3.57498400	C	-1.04344600	0.23032900	-3.56848000
C	1.77304000	-0.39372600	4.77312400	C	-1.80027500	0.45796000	-4.76664300
C	1.25090200	-0.11917200	5.98917100	C	-1.27813800	0.18341000	-5.98267500
C	-0.07675800	0.40799800	6.11132100	C	0.04954200	-0.34376600	-6.10482800
C	-0.82886600	0.63956600	5.01244400	C	0.80164500	-0.57533700	-5.00596400
C	-0.32159900	0.36533100	3.69808900	C	0.29438200	-0.30110500	-3.69158700
C	-1.06796600	0.59268100	2.56461900	C	1.04074100	-0.52845300	-2.55814400
C	-0.56169000	0.32020900	1.27583800	C	0.53446900	-0.25598000	-1.26932600
H	2.28671300	-0.88163600	-0.20831800	H	-2.31394000	0.94586800	0.21481300
H	2.52955400	-0.83629700	2.23449300	H	-2.55678600	0.90052900	-2.22799900
H	2.77524500	-0.79175900	4.67718900	H	-2.80248100	0.85598900	-4.67069600
H	1.83235200	-0.29542100	6.88373300	H	-1.85957400	0.35965700	-6.87724800
H	-0.47151100	0.61902800	7.09572100	H	0.44428300	-0.55478600	-7.08923400
H	-1.83184300	1.03740500	5.10088600	H	1.80462100	-0.97317900	-5.09439500
H	-2.07153000	0.99113200	2.65762000	H	2.04430600	-0.92690500	-2.65112800

2. The Cartesian coordinates of pentacene dimer structure (in Å) with DMRG(22π22e)/NEVPT2/cc-pVTZ (M=1000) energies of -1688.9122476, -1688.8444652, -1688.8413507, -1688.8392253, -1688.8329462, -1688.8077224 E_h for S_0-S_5 states, respectively.

C	-0.72537787	0.32890493	-1.16524187	C	2.24846286	3.41094746	-1.13506502
C	-0.51023340	0.38305041	1.25899737	C	2.50212283	3.48153794	1.28502348
C	0.51023340	-0.38305041	-1.25899737	C	3.48339217	4.11441606	-1.28502248
C	0.72537787	-0.32890493	1.16524187	C	3.73705214	4.18500654	1.13506602
C	-1.20766964	0.69585546	0.09163535	C	1.78575440	3.11041636	0.14656688
C	1.20766964	-0.69585546	-0.09163535	C	4.19976060	4.48553764	-0.14656588
C	0.29160582	-0.43556160	-3.68807885	C	3.22617016	4.04195114	-3.70980658
C	0.93793954	-0.27289858	3.59478361	C	3.98821158	4.25401797	3.56058630
C	-0.93793954	0.27289858	-3.59478361	C	1.99730342	3.34193603	-3.56058530
C	-0.29160582	0.43556160	3.68807885	C	2.75934484	3.55400286	3.70980758
C	0.99088295	-0.75068114	-2.53803636	C	3.94410651	4.41448611	-2.58879292
C	1.42510113	-0.64140131	2.35471673	C	4.45605913	4.55695627	2.29558290
C	-1.42510113	0.64140131	-2.35471673	C	1.52945587	3.03899773	-2.29558190
C	-0.99088295	0.75068114	2.53803636	C	2.04140849	3.18146789	2.58879392
C	0.07391953	-0.48762907	-6.10372002	C	2.97010282	3.96973480	-6.12116200
C	1.14906028	-0.21704806	6.01092297	C	4.23771700	4.32249635	5.97273853
C	-1.14906028	0.21704806	-6.01092297	C	1.74779800	3.27345765	-5.97273753
C	-0.07391953	0.48762907	6.10372002	C	3.01541218	3.62621920	6.12116300
C	0.77459321	-0.80620762	-4.99015421	C	3.68885920	4.34383827	-5.03677250
C	1.64403085	-0.58739597	4.80663426	C	4.71394497	4.62910712	4.74324210
C	-1.64403085	0.58739597	-4.80663426	C	1.27157003	2.96684688	-4.74324110
C	-0.77459321	0.80620762	4.99015421	C	2.29665580	3.25211573	5.03677350
H	-2.13551484	1.23047695	0.16203823	H	0.85842130	2.58216773	0.25917293
H	2.13551484	-1.23047695	-0.16203823	H	5.12709370	5.01378627	-0.25917193
H	-2.35301943	1.17587141	-2.28695991	H	0.60200773	2.51076386	-2.18562471
H	-1.91833375	1.28526889	2.61106092	H	1.11451154	2.65338742	2.70400983
H	1.91833375	-1.28526889	-2.61106092	H	4.87100346	4.94256658	-2.70400883
H	2.35301943	-1.17587141	2.28695991	H	5.38350727	5.08519014	2.18562571
H	-1.68534529	0.45758427	-6.90843347	H	1.19695718	2.98808577	-6.84802130
H	-0.44479268	0.76979454	7.07006372	H	2.65959552	3.39512017	7.10654218
H	0.44479268	-0.76979454	-7.07006372	H	3.32591948	4.20083383	-7.10654118
H	1.68534529	-0.45758427	6.90843347	H	4.78855782	4.60786823	6.84802230
H	-2.57159898	1.12174357	-4.73781787	H	0.34448907	2.43878927	-4.63223774
H	-1.70188534	1.34062468	5.06208058	H	1.36990024	2.72414869	5.15088151
H	1.70188534	-1.34062468	-5.06208058	H	4.61561476	4.87180531	-5.15088051
H	2.57159898	-1.12174357	4.73781787	H	5.64102593	5.15716473	4.63223874

References

[1] E. Heinecke, D. Hartmann, R. Müller and A. Hese, *J. Chem. Phys.*, 1998, **109**, 906–911.

[2] P. M. Zimmerman, Z. Zhang and C. B. Musgrave, *Nat. Chem.*, 2010, **2**, 648–642.

[3] T. Zeng, R. Hoffmann and N. Ananth, *J. Am. Chem. Soc.*, 2014, **136**, 5755–5764.

[4] Y. Kurashige and T. Yanai, *Bull. Chem. Soc. Jpn.*, 2014, **87**, 1071–1073.

[5] P. M. Zimmerman, F. Bell, D. Casanova and M. Head-Gordon, *J. Am. Chem. Soc.*, 2011, **133**, 19944–19952.

[6] Z. Li, S. Guo, Q. Sun and G. K.-L. Chan, *Nat. Chem.*, 2019, **11**, 1026–1033.

[7] A. E. Clark and E. R. Davidson, *J. Chem. Phys.*, 2001, **115**, 7382–7392.

[8] A. V. Luzanov, D. Casanova, X. Feng and A. I. Krylov, *J. Chem. Phys.*, 2015, **142**, 224104.

[9] F. Plasser and H. Lischka, *J. Chem. Theory Comput.*, 2012, **8**, 2777–2789.

[10] A. J. Stone, *The Theory of Intermolecular Forces, 2nd ed*, 2013, University Press: Oxford, U.K.

[11] B. Błasiak, M. Maj, M. Cho and R. W. Góra, *J. Chem. Theory Comput.*, 2015, **11**, 3259–3266.

[12] S. Ito, T. Nagami and M. Nakano, *J. Phys. Chem. Lett.*, 2015, **6**, 4972–4977.

[13] K. Tokunaga, T. Sato and K. Tanaka, *J. Chem. Phys.*, 2006, **124**, 154303.

[14] T. Sato, K. Tokunaga and K. Tanaka, *J. Chem. Phys.*, 2006, **124**, 024314.

[15] M. E. Peskin and D. V. Schroeder, *An Introduction To Quantum Field Theory (Frontiers in Physics)*, 1995, Westview Press.

[16] P. Giannozzi, S. Baroni, N. Bonini, M. Calandra, R. Car, C. Cavazzoni, D. Ceresoli, G. L. Chiarotti, M. Cococcioni, I. Dabo, A. D. Corso, S. de Gironcoli, S. Fabris, G. Fratesi, R. Gebauer, U. Gerstmann, C. Gougoussis, A. Kokalj, M. Lazzeri, L. Martin-Samos, N. Marzari, F. Mauri, R. Mazzarello, S. Paolini, A. Pasquarello, L. Paulatto, C. Sbraccia, S. Scandolo, G. Sclauzero, A. P. Seitsonen, A. Smogunov, P. Umari and R. M. Wentzcovitch, *J. Phys.: Condens. Matter*, 2009, **21**, 395502.

[17] X. Gonze and C. Lee, *Phys. Rev. B*, 1997, **55**, 10355–10368.